

## Numerical prediction of vortex dynamics in inviscid sheet cavitation

Schenke, Sören; van Terwisga, Thomas

**Publication date**

2017

**Document Version**

Accepted author manuscript

**Published in**

Proceedings of the 20th Numerical Towing Tank Symposium (NuTTS 2017)

**Citation (APA)**

Schenke, S., & van Terwisga, T. (2017). Numerical prediction of vortex dynamics in inviscid sheet cavitation. In T. Lloyd, & A. van der Ploeg (Eds.), *Proceedings of the 20th Numerical Towing Tank Symposium (NuTTS 2017)* (pp. 197-202). Curran.

**Important note**

To cite this publication, please use the final published version (if applicable). Please check the document version above.

**Copyright**

Other than for strictly personal use, it is not permitted to download, forward or distribute the text or part of it, without the consent of the author(s) and/or copyright holder(s), unless the work is under an open content license such as Creative Commons.

**Takedown policy**

Please contact us and provide details if you believe this document breaches copyrights. We will remove access to the work immediately and investigate your claim.

# Numerical Prediction of Vortex Dynamics in Inviscid Sheet Cavitation

Sören Schenke\*, Tom J.C. van Terwisga<sup>†\*</sup>

\*TU Delft, Delft/ the Netherlands, <sup>†</sup>MARIN, Wageningen/ the Netherlands  
s.schenke@tudelft.nl

## 1 Introduction

Recent studies have indicated that mass transfer models are able to correctly reflect the sheet cavitation dynamics of inertia driven flows, given that the mass transfer model constants governing the source term magnitude are sufficiently large (Koukouvinis and Gavaises 2015) and that enough temporal resolution is provided (Schenke and Van Terwisga 2017). The inertia driven dynamics, characterised by cavity collapse time, shedding frequencies and local pressure impact frequencies, were shown to be insensitive to variations of the mass transfer coefficients in this limit.

This study focuses on an inviscid cavitating flow around a NACA0015 hydrofoil. The flow dynamics are driven by the re-entrant jet as the main mechanism of cavity shedding. A threshold of mass transfer magnitude, temporal and spanwise spatial resolution is identified, beyond which the frequency of local pressure impacts is model parameter independent. Although the exact values of peak pressure loads remain time step size, grid size and model parameter dependent, the sheet cavitation dynamics are considered as well resolved in this regime as far as shedding frequency and characteristic cavity collapse time are concerned. The results are compared to experimental results by Van Rijsbergen et al. (2012). Based on this, the study further focuses on the mechanism of vorticity generation and vorticity break-up, causing potentially erosive cavitating structures such as horseshoe cavities (Dular and Petkovšek 2015).

## 2 Modelling Approach

The vorticity equation, as derived from the inviscid Navier-Stokes equation for momentum without any non-conservative body forces but with variable density, is given by (Xing et al. 2005)

$$\frac{\partial \omega}{\partial t} + u \cdot \nabla \omega = \omega \cdot \nabla u - \omega \nabla \cdot u + \frac{1}{\rho^2} \nabla \rho \times \nabla p, \quad (1)$$

where  $\omega = \nabla \times u$  denotes the vorticity. The term  $\omega \cdot \nabla u$  on the right-hand side represents the three-dimensional tilting of vorticity vectors and the divergence term  $\omega \nabla \cdot u$  reflects the alteration of vorticity due to density change. The baroclinic term  $1/\rho^2 \nabla \rho \times \nabla p$  must always be zero in an ideal barotropic flow (Koop 2008). Mass transfer models, however, typically generate artificial baroclinic torque, because the density-pressure states can not follow unique barotropic states (Schenke and Van Terwisga 2017). Similar to a study on cavitating vortices by Xing et al. (2005), the vorticity Eq. (1) is only employed for post-processing purposes. The flow model itself is based on the inviscid Navier-Stokes equations for momentum and mass continuity:

$$\rho \frac{\partial u}{\partial t} + \rho u \cdot \nabla u = -\nabla p + \rho g \quad (2)$$

$$\frac{\partial \rho}{\partial t} + \nabla \cdot (\rho u) = 0 \quad (3)$$

The velocity field is modeled as divergence free in the incompressible pure liquid and vapour regimes with corresponding densities  $\rho_l$  and  $\rho_v$ . In the phase transition regime, the local velocity divergence is equal to a mass transfer source term, for which the model by Merkle et al. (1998), slightly modified however (Schenke and Van Terwisga 2017), is employed:

$$\nabla \cdot u = -\frac{1}{\rho} \left( 1 - \frac{\rho_v}{\rho_l} \right) (p - p_v) \begin{cases} C_v \gamma & \text{if } p \leq p_v \\ C_c (1 - \gamma) & \text{if } p > p_v \end{cases} \quad (4)$$

With the liquid volume fraction  $\gamma$  given by the linear mixture relation  $\gamma = (\rho - \rho_v) / (\rho_l - \rho_v)$ , combining Eq. (3) and Eq. (4) gives the liquid volume fraction transport equation:

$$\frac{\partial \gamma}{\partial t} + \nabla \cdot (\gamma u) = -\frac{1}{\rho} \frac{\rho_v}{\rho_l} (p - p_v) \begin{cases} C_v \gamma & \text{if } p \leq p_v \\ C_c (1 - \gamma) & \text{if } p > p_v \end{cases} \quad (5)$$

### 3 Numerical Set-Up

The numerical set-up is in line with experiments carried out by Van Rijsbergen et al. (2012) and numerical simulations carried out by Li et al. (2014), where the open source CFD package OpenFOAM (2017) is employed in this study. The angle of attack of the NACA0015 hydrofoil is  $8^\circ$  and its cord length is  $c = 0.06$  m, with the channel height and width being 0.08 m and 0.04 m, respectively. The inlet is located at  $3c$  upstream from the leading edge of the foil and the outflow enters a diffuser section (Fig. 2) at  $6.5c$  downstream from the leading edge to avoid pressure fluctuations at the outlet boundary. The ratio between the diffuser outlet patch and the tunnel cross section area is 66. The inflow boundary condition is given by a uniform inflow speed of 17.3 m/s and the downstream pressure in the foil tunnel section is aimed to be 302.295 kPa. The fixed outlet pressure at the end of the diffuser section is derived from the Bernoulli equation and the mass continuity equation. By this means, the aimed downstream tunnel pressure is matched under wetted flow conditions. The vapour pressure is  $p_v = 1854$  Pa and the densities of pure liquid and vapour are  $\rho_l = 998.85$  kg/m<sup>3</sup> and  $\rho_v = 0.01389$  kg/m<sup>3</sup>, respectively. Since viscous forces are neglected, any solid wall is treated as a slip wall. The numerical simulation is carried out on an unstructured grid with uniform grid density around the foil. Four refinement levels are applied in the vicinity of the foil (Fig. 1). The refinement factors against the background mesh are  $2^n$ , where  $n = 0$  on the base level and  $n = 4$  on the finest level around the foil. On the finest level, the cell length in axial direction is  $\Delta x = 0.3125$  mm. To investigate the effect of three-dimensional vorticity break-up, the spanwise resolution is varied, where  $\Delta z = 8\Delta x$  for the coarse grid,  $\Delta z = 4\Delta x$  for the medium grid and  $\Delta z = 2\Delta x$  for the fine grid. The mass transfer constants  $C_{c,v}$  and time step size  $\Delta t$  have been varied systematically to identify a converged configuration for a given grid density. In all cases, the ratio between  $C_c$  and  $C_v$  is kept constant at  $C_c/C_v = 2$ . Local quantities such as pressure and density signals are evaluated at observation points on the foil surface at  $0.2c$  and  $0.5c$  in the centre plane.

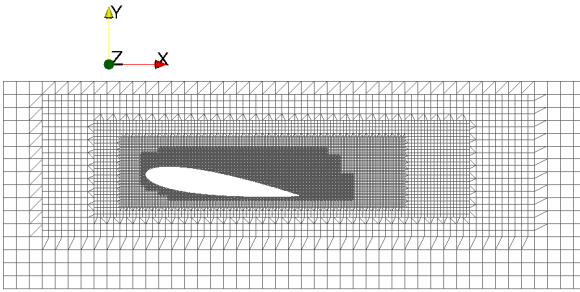


Fig. 1: Unstructured grid with 4 refinement levels

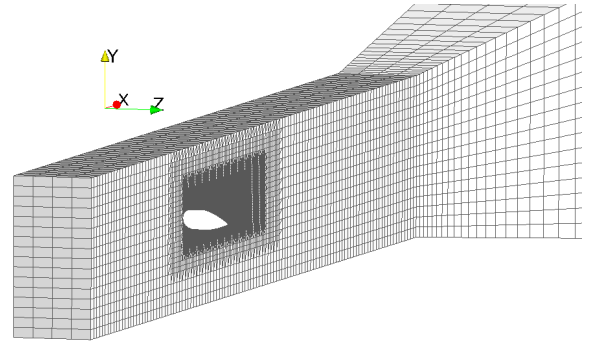


Fig. 2: Foil and diffuser section

### 4 Results

The local main pressure impacts at  $0.2c$  and  $0.5c$  (Fig. 3) show strong correlation. The dominating frequency of the cyclic pressure loads is identified from Fast Fourier Transforms of the pressure signals (Fig 4) at  $0.2c$ . Subfigures A, B and C depict the pressure amplitude spectra for decreasing time step size and three different mass transfer rates each, where the data is obtained from the finest grid ( $\Delta z = 2\Delta x$ ). The dominating frequency gets more pronounced with decreasing time step size. The same effect is observed for variation of the spanwise resolution (subfigure D), where the dominating frequency band is smeared out as the spanwise resolution decreases. From subfigure C we find a model parameter independent pressure load frequency of 193 Hz. This value is in good agreement with the shedding frequency of 188 Hz that was found by Van Rijsbergen et al. (2012) from their experiments. Convergence of the impact frequency is confirmed by Fig. 3, depicting the pressure signals for two different mass transfer constants differing by a factor of 100. While the frequency converges to a model parameter independent value, the impact amplitudes still exhibit strong dependency on the magnitude of the mass transfer constants  $C_{c,v}$  and temporal resolution. They increase with increasing  $C_c$  and decreasing  $\Delta t$ .

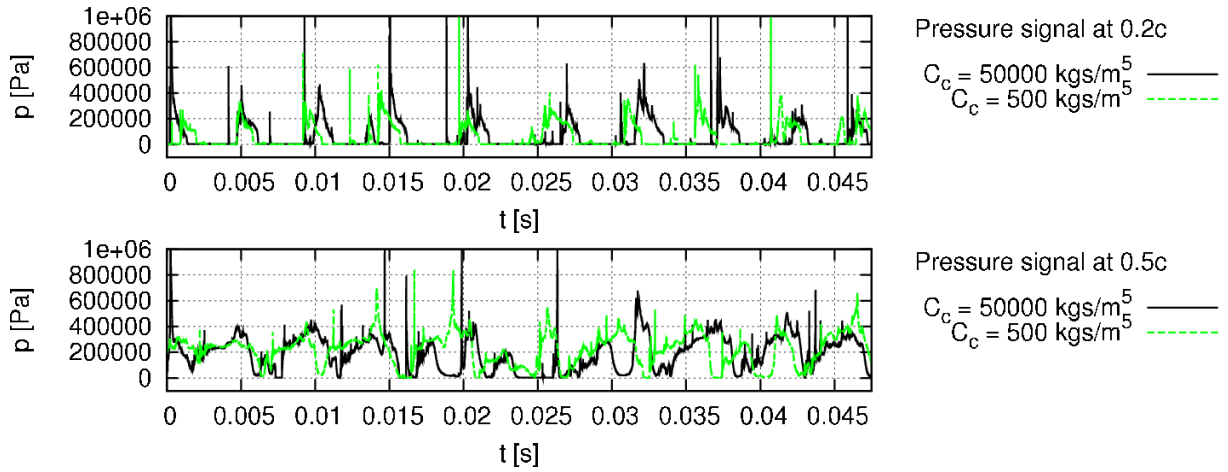


Fig. 3: Pressure signals on the foil surface at  $0.2c$  (above) and  $0.5c$  (below) in the centre plane for  $\Delta t = 7.5e-7$  s (small time step) and  $\Delta x/\Delta z = 1/2$  (fine grid)

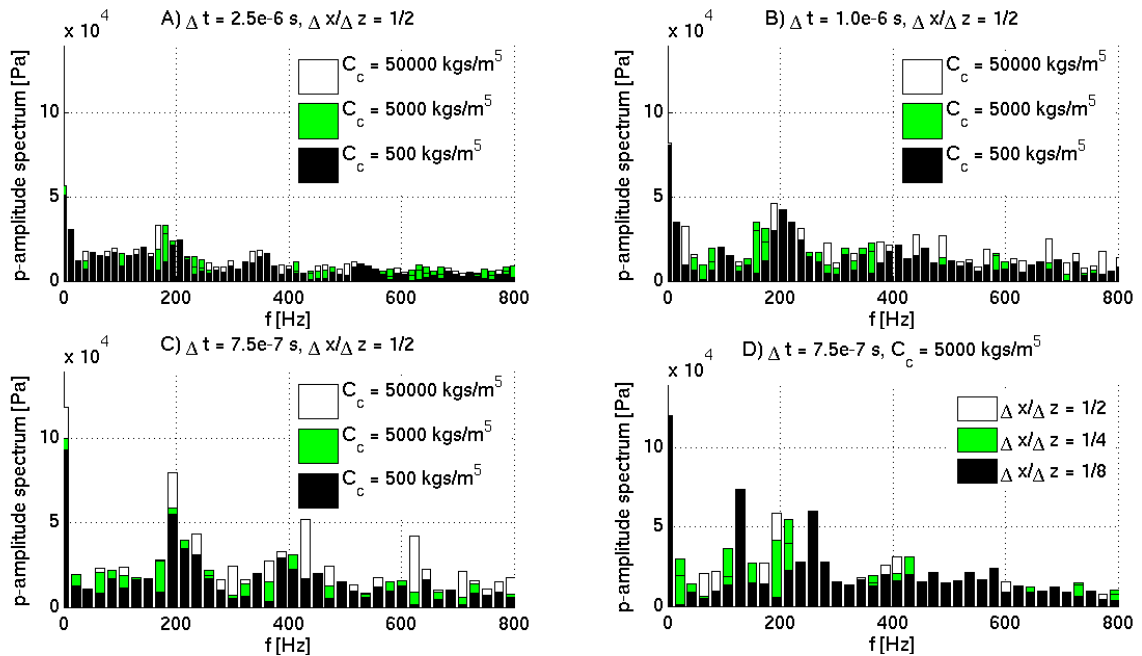


Fig. 4: Pressure amplitude spectra on the foil surface at  $0.2c$  in the centre plane

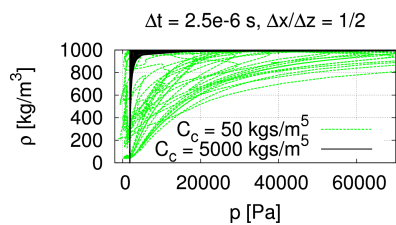


Fig. 5:  $\rho$ - $p$  trajectory for large time step and fine grid

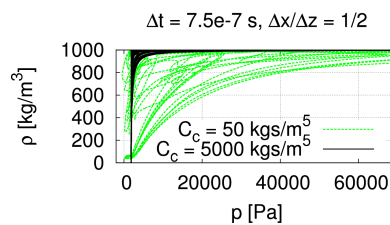


Fig. 6:  $\rho$ - $p$  trajectory for small time step and fine grid

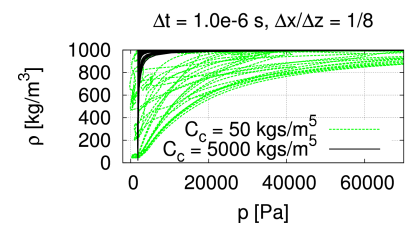


Fig. 7:  $\rho$ - $p$  trajectory for medium  $\Delta t$  and coarse grid

Obviously, variation of the mass transfer coefficients does not affect the inertia driven dynamics of the flow as long as they are sufficiently large. Increasing the mass transfer constants  $C_{c,v}$  has the effect of increasing the steepness of the density-pressure trajectories (Koukouvinis and Gavaises 2015, Schenke and Van Terwisga 2017). As shown by Fig. 5, 6 and 7, the outline of the area swept by the trajectories on statistical average only depends on the values of the mass transfer constants and is independent from both

time step size (compare Fig. 5 and Fig. 6) and grid density (compare with Fig. 7). Temporal resolution, however, has an influence on the time that it takes to achieve phase transition, hence the time that it takes to cover the same trajectory. With decreasing time step size, this characteristic phase transition time converges to a limit value (Schenke and Van Terwisga 2017).

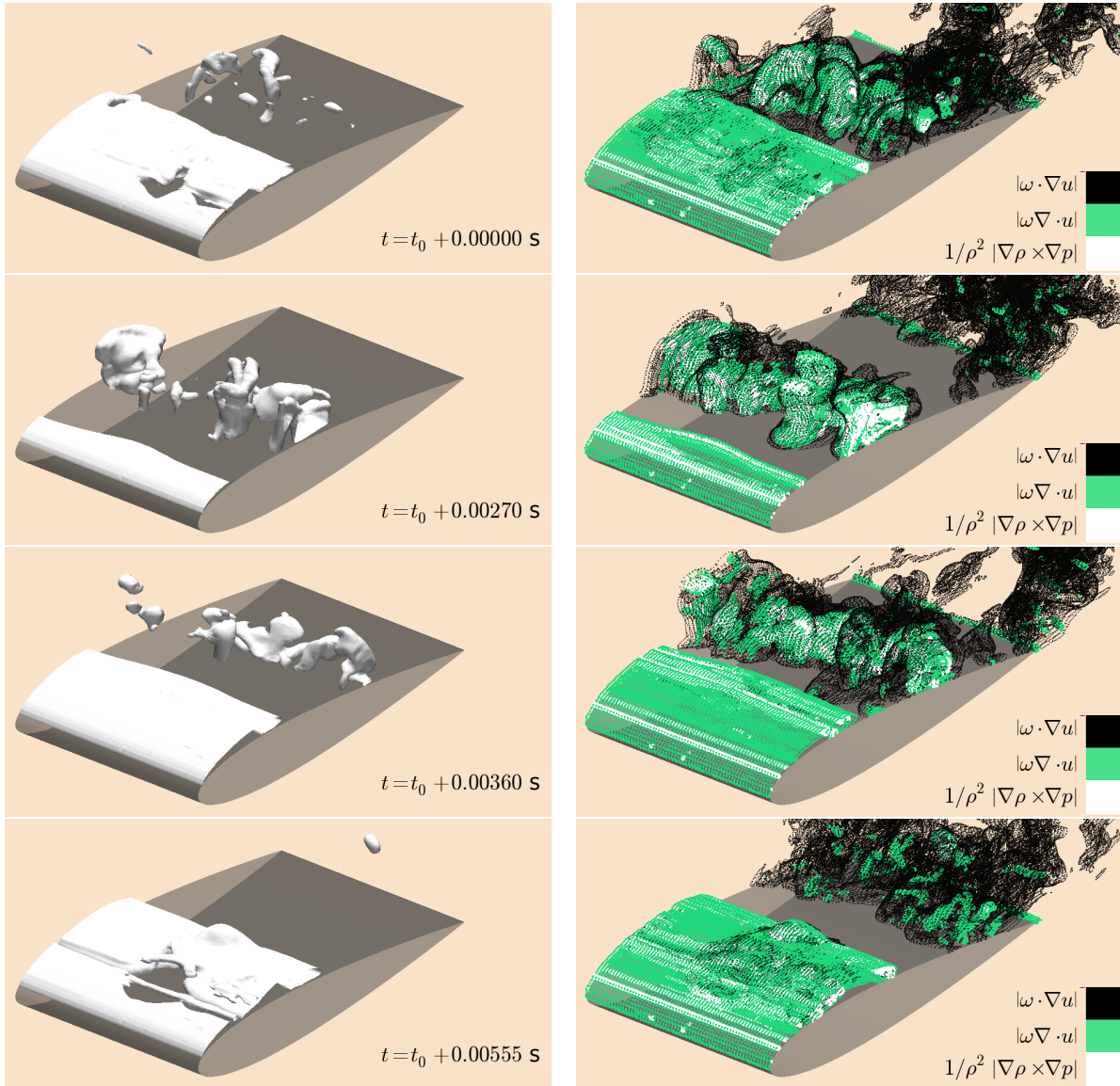


Fig. 8: Instantaneous vapour structures indicated by iso-surfaces at  $\gamma = 0.75$  (left) and corresponding iso-surfaces of the vorticity equation source term magnitudes at  $1.0e7 \text{ s}^{-2}$  (right)

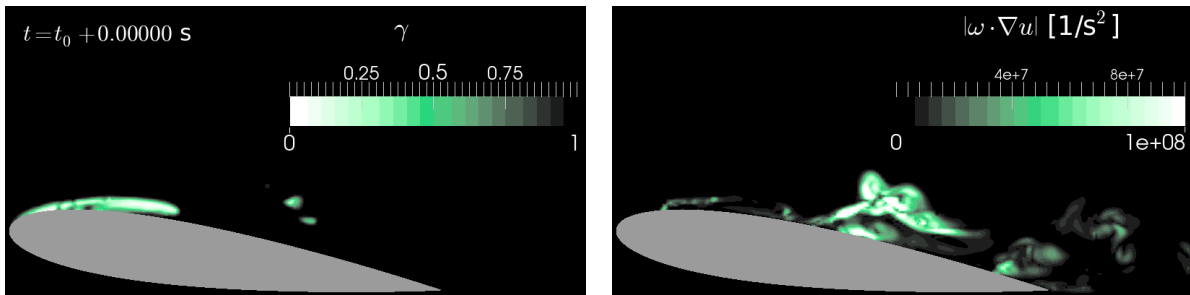


Fig. 9: Instantaneous volume fraction field in the centre plane (left) and corresponding magnitude of the vortex tilting source term  $\omega \cdot \nabla u$  (right)

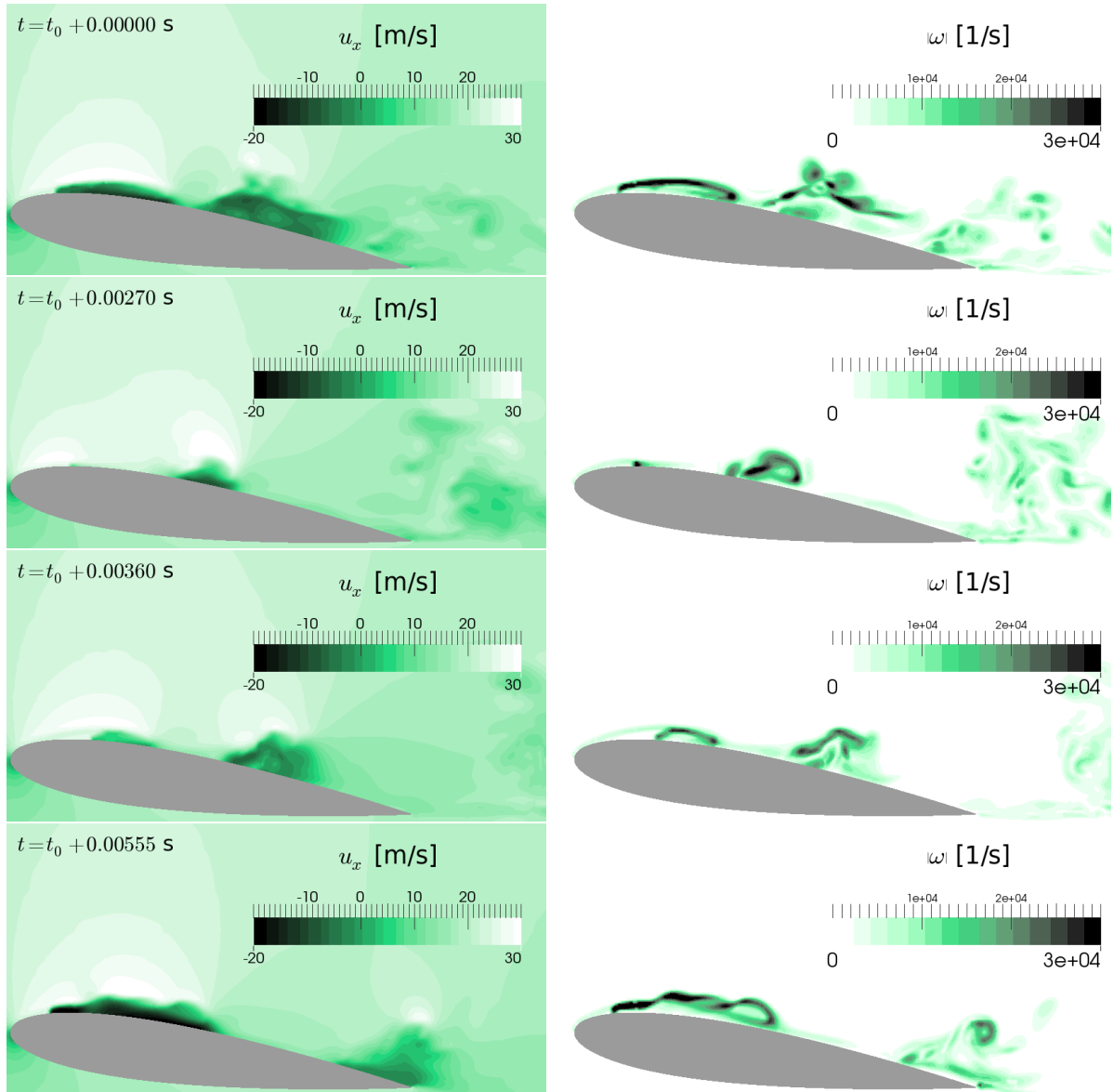


Fig. 10: Axial velocity field in the centre plane (left) and corresponding vorticity magnitude field (right)

The converged simulation for  $\Delta t = 7.5e-7$  s and  $C_c = 50000$  kgs/m<sup>5</sup> is extended a little further to investigate the formation of cavitating vortical structures. Schmidt et al. (2009) have shown that the formation of vortical structures in sheet cavitation is mainly an inertia driven effect. The alteration of the vorticity field is visualised by evaluating iso-surfaces of the source terms on the right-hand side of the vorticity Eq. (1). Fig. 8 (right) depicts instantaneous iso-surfaces of the source term magnitudes at  $1.0e7$  s<sup>-2</sup> for one shedding cycle, from the time instant of cavity pinch-off to the subsequent pinch-off. The white iso-surface represents the artificial baroclinic torque contribution, the green iso-surface the divergence contribution, in this case associated with phase transition, and the black iso-surface the three-dimensional tilting of vorticity vectors. The corresponding instantaneous vapour structures are shown in Fig. 8 (left). During the growing phase at instants  $t_0 + 0.00270$  s and  $t_0 + 0.00360$  s, the sheet cavity exhibits two-dimensional behaviour. Spanwise disturbances at the specified iso-surface magnitude are observed downstream from the pinch-off region at instants  $t_0 + 0.00000$  s and  $t_0 + 0.00555$  s. The main three-dimensional break-up, however, occurs as the shed cavities collapse further downstream. The inception region of the spanwise instability, indicated by the formation of vortex tilting in Fig. 9 (right) coincides with the pinch-off region indicated by the volume fraction field in Fig. 9 (left). The vorticity break-up associated with the downstream cavity collapse, however, is significantly larger. Prior to the occurrence of spanwise instabilities, we observe the formation of large in-plane vorticity caused by the re-entering

flow. Fig. 10 (left) depicts the distribution of the axial velocity component in the centre plane and Fig. 10 (right) shows the corresponding distribution of vorticity magnitude. At the moment of pinch-off (instants  $t_0 + 0.00000$  s and  $t_0 + 0.00555$  s), a re-entrant flow velocity in the order of 20 m/s is observed, going along with the generation of pronounced in-plane vorticity around the sheet. This in-plane vorticity is almost zero during the sheet growing phase at instant  $t_0 + 0.00270$  s and builds up as the re-entrant jet starts to form at instant  $t_0 + 0.00360$  s. An overview over different mechanisms possibly causing the formation of vorticity in the pinch-off region is given by Dular and Petkovšek (2015). A comparison of Fig. 8 and 10 further shows that the three-dimensional break-up of vorticity goes along with the formation of cavitating ring structures such as horseshoe cavities observed at instants  $t_0 + 0.00000$  s and  $t_0 + 0.00360$ .

## 5 Conclusion

We have identified a configuration of mass transfer magnitude, temporal and spatial resolution for which the sheet cavitation dynamics around a NACA0015 hydrofoil are not sensitive to variation of the mass transfer model constants, given that the model constants are sufficiently large to provide an overcapacity of mass transfer magnitude which is not fully exploited during phase transition. In this regime the mass transfer constants could be varied by a factor of 100 without having any effect on the dominating frequency of the cyclic sheet cavitation dynamics. The predicted frequency is in good agreement with experimental results by Van Rijsbergen et al. (2012). We conclude that the cavitation dynamics of the larger scale structures are correctly predicted. Local peak pressures, however, remain dependent on both resolution and mass transfer magnitude and are not reliably predicted. The results further suggest that the inception of spanwise instabilities occurs in the cavity pinch-off region, even in the absence of viscous forces, and that the break-up of vorticity is amplified during the collapse of the shed cavities. This confirms the finding by Schmidt et al. (2009), stating that sheet cavitation dynamics are inertia driven.

## Acknowledgements

We greatly appreciate the financial support of this research provided by the EU CaFE ITN initiative and the MARIN Academy. We also thank the members of the CaFE project as well as the involved MARIN researchers for the inspiring discussions on cavitation.

## References

- M. Dular and M. Petkovšek (2015). On the Mechanisms of Cavitation Erosion - Coupling High Speed Videos to Damage Patterns. *Experimental Thermal and Fluid Science*, **68**(2015), 359–370.
- A.H. Koop (2008). *Numerical Simulation of Unsteady Three-Dimensional Sheet Cavitation*. PhD thesis, University of Twente.
- P. Koukouvinis and M. Gavaises (2015). Simulation of Throttle Flow with Two Phase and Single Phase Homogeneous Equilibrium Model. Proceedings of the 9th International Symposium on Cavitation, Lausanne, Switzerland.
- Z. Li, M. Pourquie and T.J.C. van Terwisga (2014). Assessment of Cavitation Erosion With a URANS Method. *Journal of Fluids Engineering*, **136**(4), 041101-1–041101-11.
- C.L. Merkle, J.Z. Feng and P.E.O. Buelow (1998). Computational Modeling of the Dynamics of Sheet Cavitation. Proceedings of the 3rd International Symposium on Cavitation, Grenoble, France.
- OpenFOAM (2017). OpenFOAM web site, 2017.
- M. van Rijsbergen, E.J. Foeth, P. Fitzsimmons and A. Boorsma (2012). High-Speed Video Observations and Acoustic-Impact Measurements on a NACA 0015 Foil. Proceedings of the 8th International Symposium on Cavitation, Singapore, Republic of Singapore.
- S. Schenke and T.J.C. van Terwisga (2017). Simulating Compressibility in Cavitating Flows with an Incompressible Mass Transfer Flow Solver. Proceedings of the 5th International Symposium on Marine Propulsors, Espoo, Finland.
- S.J. Schmidt, M. Thalhamer and G.H. Schnerr (2009). Inertia Controlled Instability and Small Scale Structures of Sheet and Cloud Cavitation. Proceedings of the 7th International Symposium on Cavitation, Ann Arbor, Michigan, USA.
- T. Xing, Z. Li and S.H. Frankel (2005). Numerical Simulation of Vortex Cavitation in a Three-Dimensional Submerged Transitional Jet. *Journal of Fluids Engineering*, **127**(4), 714–725.